




Fine-grained domain counting and percolation analysis in two-dimensional lattice systems with linked lists

Hrushikesh Sable ^{1,2,3}, Deepak Gaur ^{1,2} and D. Angom ^{1,4}

¹*Physical Research Laboratory, Ahmedabad 380009, Gujarat, India*

²*Indian Institute of Technology Gandhinagar, Palaj, Gandhinagar 382355, Gujarat, India*

³*Department of Physics, Virginia Tech, Blacksburg, Virginia 24061, USA*

⁴*Department of Physics, Manipur University, Canchipur 795003, Manipur, India*



(Received 13 April 2023; accepted 25 September 2023; published 20 October 2023)

We present a fine-grained approach to identify clusters and perform percolation analysis in a two-dimensional (2D) lattice system. In our approach, we develop an algorithm based on the linked-list data structure whereby the members of a cluster are nodes of a path. This path is mapped to a linked-list. This approach facilitates unique cluster labeling in a lattice with a single scan. We use the algorithm to determine the critical exponent in the quench dynamics from the Mott insulator to the superfluid phase of bosons in 2D square optical lattices. The results obtained are consistent with the Kibble-Zurek mechanism. We also employ the algorithm to compute the correlation length using definitions based on percolation theory and use it to identify the quantum critical point of the Bose Glass to superfluid transition in the disordered 2D square optical lattices. In addition, we compute the critical exponent ν which quantify the divergence of the correlation length ξ across the phase transition and the fractal dimension of the hulls of the superfluid clusters.

DOI: [10.1103/PhysRevE.108.045307](https://doi.org/10.1103/PhysRevE.108.045307)

I. INTRODUCTION

There are strong motivations across research disciplines to develop novel approaches and computational methods to study the percolation theory. The percolation theory provides a simple and unifying framework to understand clustering of particles in a medium. It has wide applications like the permeation of fluid in porous media [1], spontaneous magnetization of dilute ferromagnets [2], and polymer gels [3], to mention a few. The study of the clustering or connectivity of the particles gains importance as it determines the macroscopic properties of the system. For example, the electrical conduction through a composite mixture of conducting and insulating materials is described by the percolation analysis of the conducting material in the mixture.

A generic percolation problem consists of an infinite lattice populated with two classes of lattice sites at random. These are denoted as occupied and unoccupied sites [4,5]. A group of occupied sites connected through bonds forms a cluster. The probability of a site being occupied determines the distribution and size of the clusters. The system undergoes a percolation phase transition when the probability exceeds a critical value. Then, there exists a spanning cluster which extends from one edge of the system to the opposite edge. Although the percolation problem as stated is straightforward, analytical approaches are limited. It is, however, possible to gain an understanding of the system using numerical methods. A prominent algorithm used in percolation analysis is the Hoshen-Kopelman (HK) cluster multiple labeling algorithm [6]. The application of the percolation analysis and of the HK algorithm are in diverse fields like food and chemical engineering [7,8], ecology [9], and biology [10]. The basic essence of the algorithm is to scan through the lattice and identify the

occupied sites. During the scan, the occupancy of neighboring sites are also checked and the connected occupied sites are assigned a cluster label. The key point of the algorithm is that the neighboring sites are allowed to have different labels, but with a record that they belong to the same cluster. There are now several variations of the HK [11–15] including a proposal to use linked-list to group the clusters belonging to the same domain [16].

In this work, we present a fine-grained algorithm of cluster labeling and describe its application in the percolation analysis of two-dimensional (2D) lattices. The algorithm employs the linked-list data structure and we refer to it as domain counting (DC) algorithm. Using which we can define a path connecting all the sites belonging to a cluster. This facilitates the scanning of the lattice in a single scan. The path constructed is fine-grained as it links the sites. Such an approach facilitates the analysis of cluster properties. This is in contrast to the HK algorithm, where the equivalence class built links different cluster labels of the same underlying cluster, and is a coarse-grained linking. Different studies that can be done with this algorithm include determination of boundaries, easy identification of spanning cluster, and calculation of various cluster properties like center of mass, radius of gyration, and correlation length. Our approach is well suited for detailed analysis of results encountered in the studies of optical lattices where we obtain a set of configurations and wish to examine it using the tools from percolation theory. However, it must be emphasized that to simulate percolation the Newman-Ziff algorithm [17] is the method of choice.

We address two important problems in the physics of ultracold bosonic atoms in optical lattices using the algorithm. First, we study the quantum quench dynamics of bosons in the optical lattices from the Mott insulator (MI) to the

superfluid (SF) phase employing the time-dependent Gutzwiller mean-field theory. Using our method we identify the clusters or domains and show that the number of domains follows a power-law dependence on the quench rate. This is consistent with the Kibble-Zurek mechanism (KZM) [18–22]. It is to be mentioned that recent works on ultracold atoms have reported similar results in quantum quenches across different quantum phases [23–26]. Further, as to be expected, we show that the dependence of the defect density on the quench rate has the same power-law exponent as the number of domains. The second study pertains to the critical properties of the Bose glass (BG) to SF transition of bosons in disordered optical lattices. The BG phase is insulating yet compressible and it is characterized by the SF *puddles* with an MI background [27–30]. Using our method we compute the geometrical properties of the SF clusters. As mentioned, our fine-grained method stores locations of all the sites of a cluster. From this information, we calculate the percolation correlation length of the system across the BG-to-SF transition. As expected, the correlation length peaks at the transition point and has power-law dependence on the reduced hopping strength. The critical exponent ν which quantifies the power law reveals that the BG-to-SF transition belongs to the universality class of 2D random percolation. We also compute the fractal dimension of the hulls of SF clusters near the transition point.

The remainder of this article is organized as follows. We first introduce linked-lists and discuss mapping of the domains to a linked-list in Sec. II. We then discuss the algorithm of our method in the Sec. III. We describe the identification of the boundary of the cluster in Sec. IV. In Sec. V, we discuss the comparison of the presented algorithm with other standard algorithms in the percolation theory. In Sec. VI, we discuss the application of our method to the MI-SF quench dynamics. Then, in the Sec. VII, we present the study of the BG-to-SF transition from the perspective of percolation theory. We summarize our main results and present discussions in Sec. VIII.

II. MAPPING DOMAIN TO A LINKED-LIST

For a better description of our method, we consider a 2D square lattice and each of the lattice sites are labeled at random with either 0 or -1 . In the percolation theory, the site labeled 0 (-1) corresponds to occupied (unoccupied) site. Accordingly, we may assume that the label 0 (-1) occurs with the probability p ($1 - p$). As mentioned earlier, the task at hand is to identify and enumerate the domains with either of the two labels. For illustration let us take the domains of sites with the label 0. The lattice sites are denoted by (i, j) , where i is the column index and j is the row index. These correspond to the x - and y -axis coordinates, respectively, in the xy plane. The central idea of our approach is to use the concept of linked-list data structure [31] to describe a domain. It stores a data sequence in noncontiguous memory locations. Each element of the sequence is stored in a node of the list and each node has a reference or a link to the memory location of the next element in the sequence. This continues until the last element of the sequence. The advantage of using linked-list is the ease of updating it to insert a new node or merging multiple linked-lists. In the present work, to define a domain, each lattice site of the system is uniquely mapped to the

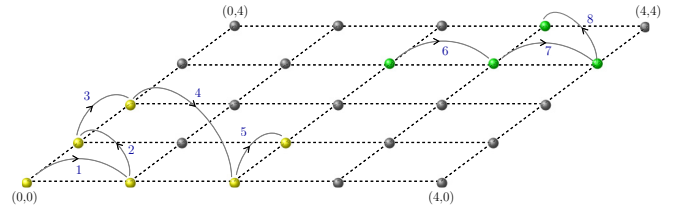


FIG. 1. A schematic diagram to illustrate the paths defining a cluster in a 2D lattice. The arrows indicate the links between sites constituting a domain. Here distinct domains are identified with different colors which are representative of domain labels, while the gray-shaded lattice sites are of label -1 . The numbers over the arrows represent the chronological sequence in linking the sites.

node of a unidirectional linked-list. The node is then linked to another lattice site which belongs to the same domain. This way each domain is represented by one linked-list. Thus, once we know the starting node of a linked-list, we can traverse through all the lattice sites belonging to a domain. For this reason, the linked-list associated with a domain can also be thought of as a *path* traversing through it. Here after, we use path to refer to the linked-list. Such a path passes through each lattice site in the domain once. Our main objective is, then, to enumerate the number of such distinct paths corresponding to the domains of lattice sites with the label 0. Then the number of such paths is the number of domains.

To define the link in the node corresponding to the (i, j) lattice site, we introduce two variables $x_{i,j}$ and $y_{i,j}$. The variable $x_{i,j}$ ($y_{i,j}$) is the location along the x (y) direction of the next lattice site in the path. These variables should have well-defined values for the lattice sites at the beginning and intermediate nodes of a path. But this is not required for the last node of a path. To distinguish the end node we assign negative integers to these two variables for this node. Since we use unidirectional linked-list it is essential to define the location of the first lattice site in a path or the first node of the path. For this we introduce two variables for each path α^k and β^k ; these are the x and y locations of the first lattice site of the k th path, respectively. To facilitate further analysis of the domains, we denote the total number of nodes or lattices sites in the k th domain by \mathcal{N}^k . The two variables γ^k and δ^k are introduced to define the x and y location of the site corresponding to the last node of the path. Suppose $\{x_{i,j}^k, y_{i,j}^k\}$ is the set of the links of the k th path, then the set of variables

$$\{\alpha^k, \beta^k, x_{i,j}^k, y_{i,j}^k, \gamma^k, \delta^k, \mathcal{N}^k\} \quad (1)$$

defines the k th path or the domain uniquely. The schematic diagram of typical paths defining clusters on a 2D square lattice are shown in Fig. 1.

III. DOMAIN IDENTIFICATION

To identify the domains, we check the label at each lattice site columnwise. We start the scan from the left edge. That is, the column scanning is done left to right or in an increasing order of the lattice site index along the x direction. During the scan, we check the label at a lattice site, say, (i, j) . If the label of the site is 0, then the variable k is incremented by 1, and the site is relabeled as k . This identifies the lattice site as a member of the k th domain and the site is linked to

the path. This number, following earlier description, is also the sequence number of the domain. There is no change in the label if the lattice site is already identified as the member of a domain. Then, we scan the label of the right nearest-neighbor lattice site $(i + 1, j)$. If the label of this site is also 0, then it is relabeled as k . This identifies the lattice site $(i + 1, j)$ as a member of the same domain. Accordingly, we update the path to include the site. Then the scan is continued to the lattice site $(i, j + 1)$, the nearest neighbor above (i, j) . In case the label of the lattice site (i, j) is -1 , then the scan proceeds to $(i, j + 1)$. That is, the label of the right nearest neighbor is not checked. This process is repeated until the topmost lattice site of the column is reached. Then we move to the next column and continue this process until the entire system is covered. Two distinct cases arise. First, the left edge column, the column scanned first. Since, this is the starting column, domains are yet to be identified. The second case concerns the columns in the bulk and the right edge column. To record the number of domains identified we use the counter κ .

A. Left edge column

At the beginning of the scan, we initialize the variable κ to zero. It is incremented by one when a new domain is encountered. For example, assume that the lattice site $(0,3)$ is the first lattice site along the column which has label 0. During the scan, on reaching this lattice site, we increment κ to 1 and relabel the lattice site $(0,3)$ as 1. This is a newly identified domain; hence, it is the first and the last node of the path for the domain with $k = 1$. Accordingly, set the first node variables $\alpha^1 = 0$ and $\beta^1 = 3$ and the last node variables $\gamma^1 = 0$ and $\delta^1 = 3$. In addition, the counter for the number of the nodes in the domain is updated as $\mathcal{N}^1 = 1$. Since this is the last node of a path we set $x_{0,3}^1 = -2$ and $y_{0,3}^1 = -2$. The choice of -2 is arbitrary. It is a number which is not assigned to any of the variables. Then we check the label of the right nearest-neighbor lattice site $(1,3)$. There are four possible outcomes as follows:

Case A: If this lattice site has 0 label, then it is relabeled as 1. The end node of the path is shifted to $(1,3)$ by assigning $x_{1,3}^1 = x_{0,3}^1$ and $y_{1,3}^1 = y_{0,3}^1$. Accordingly, update the last node variables to $\gamma^1 = 1$ and $\delta^1 = 3$. The path is then updated by linking the lattice site $(0,3)$ to $(1,3)$ by setting $x_{0,3}^1 = 1$ and $y_{0,3}^1 = 3$. Then we continue the scan along the column to the lattice site $(0,4)$ located above $(0,3)$. If this too is 0, then we extend the path to this lattice site by making this the end node with the assignment $x_{0,4}^1 = x_{1,3}^1$ and $y_{0,4}^1 = y_{1,3}^1$ and update the end node variables to $\gamma^1 = 0$ and $\delta^1 = 4$. Then connect it to the lattice site $(1,3)$ by redefining $x_{1,3}^1 = 0$ and $y_{1,3}^1 = 4$. This possibility is schematically shown in Fig. 2(a).

Case B: The lattice site $(1,3)$ is labeled zero but not $(0,4)$. This possibility is depicted schematically in Fig. 2(b). Then the last step of variable assignments in Case A is not required.

Case C: The lattice site $(1,3)$ is labeled -1 , but $(0,4)$ is labeled 0. This is similar to Case A, but without the intermediate step of linking the lattice site $(1,3)$. The situation is schematically shown in Fig. 2(c).

Case D: This is the last case and corresponds to the situation when both the lattice sites $(1,3)$ and $(0,4)$ are -1 . Then the $(0,3)$ is an isolated domain as shown in Fig. 2(d).

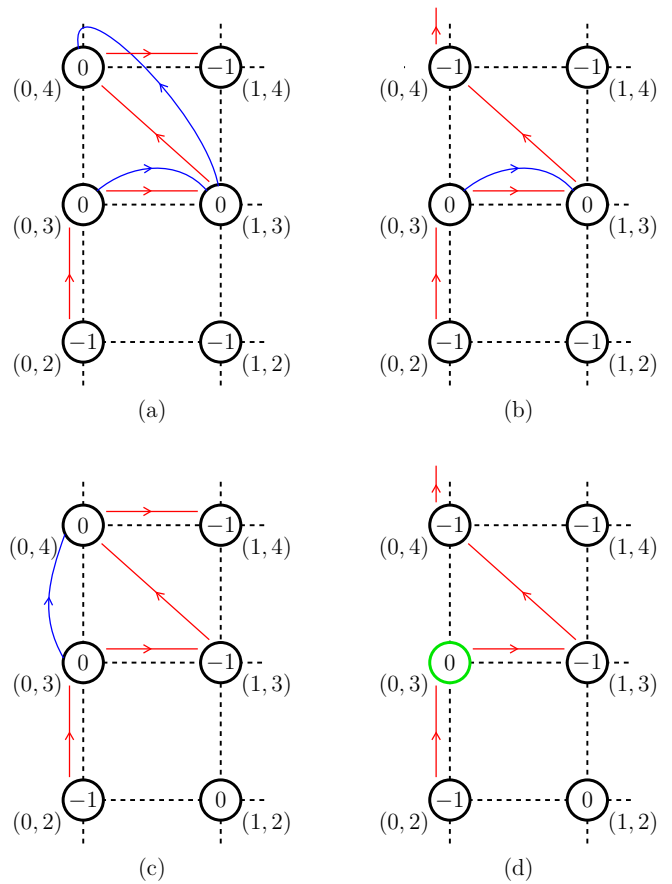


FIG. 2. A schematic diagram to illustrate the possibilities arising in the scan along the lattice sites of the leftmost column. The red arrows indicate the scanning direction, and the blue arrows represent the intersite links. The sites are represented by circles and the labels are shown within the circles. Panels (a)–(c) represent different cases of linking the site $(0,3)$ with its right and/or upper neighbors. Panel (d) represents the possibility of a domain constituting a single site.

B. Column in the bulk and right edge

The general steps of scanning the remaining columns of the system are the same. For illustration, as a general case, let us consider the scanning of the i th column and assume that we have reached the j th row in the column. That is, the lattice site to be scanned is (i, j) . If the label of the lattice site is -1 , then this is a trivial case and the site does not belong to any domain. The scan can continue to the next lattice site $(i, j + 1)$ in the column. In case the label of the lattice site (i, j) is not -1 , then there are three possible outcomes of the scan.

1. New domain

Consider that the label of the lattice site (i, j) is 0, then the current value of κ is incremented by one. The new value of κ is taken as the value of k , and the lattice site (i, j) is relabeled with this value. Like in the case of the left edge, set $x_{i,j}^k = -2$ and $y_{i,j}^k = -2$ for the path and $\mathcal{N}^k = 1$ for the number of members. The first (last) node variables of the path are set as $\alpha^k = i$ ($\gamma^k = i$) and $\beta^k = j$ ($\delta^k = j$). We then scan the lattice site $(i + 1, j)$ and followed by $(i, j + 1)$. Similar to the case of the left edge column, discussed earlier, we can

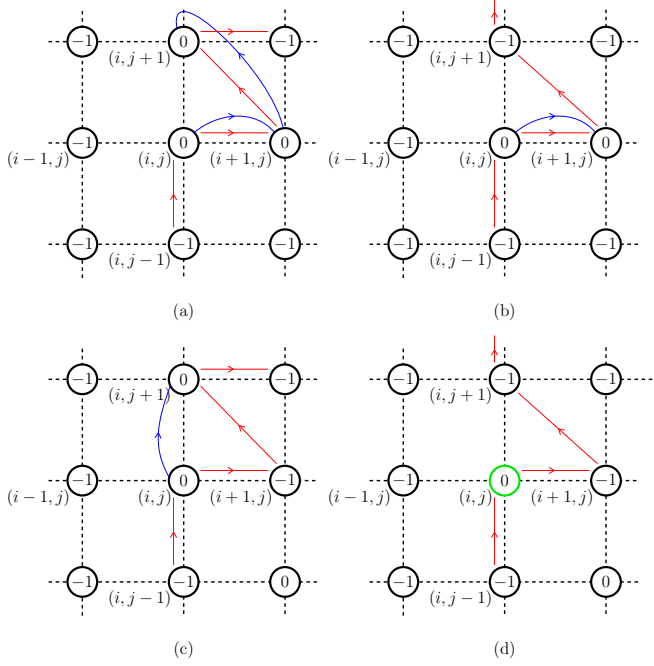


FIG. 3. A schematic diagram to illustrate the formation of a new domain comprising of sites in the bulk. The site (i, j) , labeled 0, is the starting node of the path. The steps of scanning and linking the sites in the path are similar to that in Fig. 2.

have four possible outcomes. The only difference is, in each of the cases the lattice site $(0,3)$ is replaced by (i, j) . The four cases are schematically shown in Fig. 3.

2. Old domain

Consider that the label of the lattice site is a positive integer l , indicating that (i, j) is already identified as a member of the l th domain. In this case, no modification of the variables of the lattice site are required. We then check the label of the right nearest-neighbor lattice site $(i+1, j)$. If the label is -1 , then the scan continues to the upper nearest-neighbor lattice site $(i, j+1)$. On the other hand, if the label is 0, then the lattice site belongs to the l th domain. So we have to update the domain and path variables to include $(i+1, j)$ as a part of this domain. For this, we change the label of $(i+1, j)$ to l and link the end node of the l th path to the $(i+1, j)$ by setting $x_{\gamma^l, \delta^l}^l = i+1$ and $y_{\gamma^l, \delta^l}^l = j$. Then $(i+1, j)$ is made the end node by assigning $x_{i+1, j}^l = -2$ and $y_{i+1, j}^l = -2$ and then, update the end node variables to $\gamma^l = i+1$ and $\delta^l = j$. The modifications associated with the addition of a node is complete by incrementing the node count \mathcal{N}^l by one. The schematic diagram of this possibility is shown in the Fig. 4. For illustration, the path identified in the previous column scanning is shown in light red. In general, except for the label l of site (i, j) , the three cases (A, B, and C) discussed earlier are applicable in the present case as well. Case D is not applicable, as it corresponds to a domain of isolated site. Like the earlier cases, the next step is to consider the possibility of linking the upper neighbor lattice site $(i, j+1)$. It is to be noted that the four cases shown in Fig. 3 and the case of the old

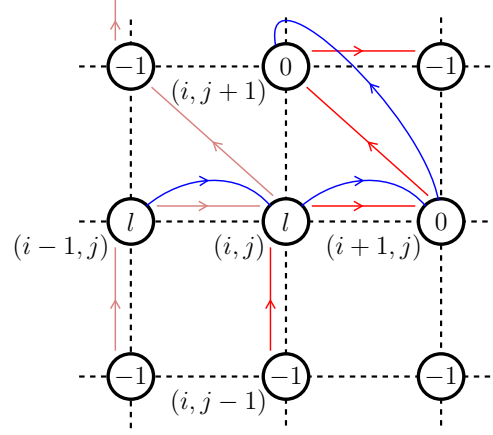


FIG. 4. A schematic diagram to illustrate the case when lattice site being scanned is already labeled with a domain label. As shown, the site (i, j) that is being scanned is labeled with label l . In this case, the right and upper neighbors are checked for label 0 and are added to the path of label l .

domain discussed covers the possibilities encountered during the scanning of the sites.

Based on the discussions, in general, appending of a site (i, j) as a new node to a path consists of three steps. First, the site (i, j) is linked to the current end node of the path. Second, the site (i, j) is identified as the end node. The addition of the node is completed by updating the end node variables and node count variable. These steps are common to all the cases.

3. Domain merging

Merging of two domains occurs when the labels of the neighboring lattice sites along the column (i, j) and $(i, j+1)$ are positive integers but different. As an example, consider the labels of these sites are l and m , respectively, and assume $l < m$. A representative case of such a situation is shown in Fig. 5. Following the conventions adopted, the domain variables of the two are $\{\alpha^l, \beta^l, x_{i, j}^l, y_{i, j}^l, \gamma^l, \delta^l, \mathcal{N}^l\}$ and $\{\alpha^m, \beta^m, x_{i, j}^m, y_{i, j}^m, \gamma^m, \delta^m, \mathcal{N}^m\}$. To merge the two domains, the first step is to link the two corresponding paths and consolidate the two into a single one. For this the last node of the l th domain is linked to the first node of the m th node. It is done by setting $x_{\gamma^l, \delta^l}^l = \alpha^m$ and $y_{\gamma^l, \delta^l}^l = \beta^m$. As a convention, we tag the merged domain with the variables corresponding to the one with the lower label value, in this case l . The merger is complete by updating the last node variables as $\gamma^l = \gamma^m$ and $\delta^l = \delta^m$, and the total number of lattice sites in the domain $\mathcal{N}^l = \mathcal{N}^l + \mathcal{N}^m$. As a last step, the m th domain is effectively nullified by setting $\mathcal{N}^m = 0$.

IV. CHARTING THE BOUNDARY

After we identify the domains, the next step is to map their boundaries. The boundary here means the outer edge of the domain. It defines the geometry of the domain. It excludes the internal boundaries associated with voids within the domains. Determining the boundary is essential to investigate the properties of the domains and to apply the methods rooted in the percolation theory. The algorithms for determining the

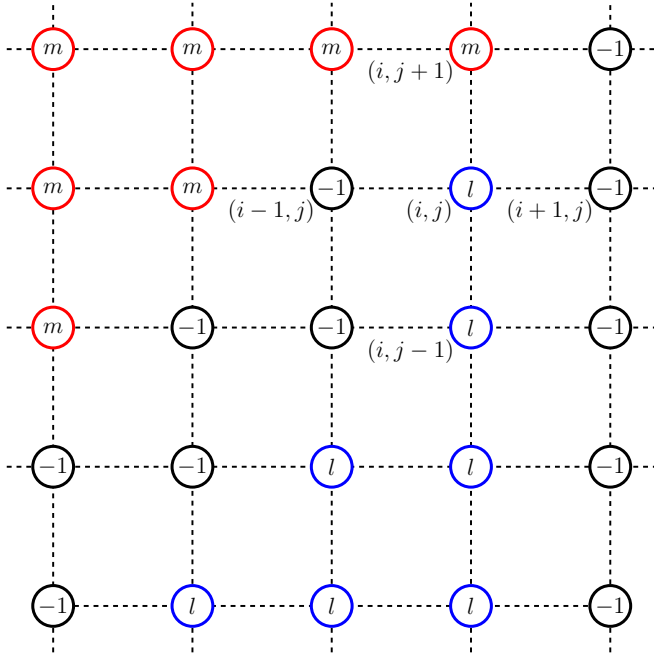


FIG. 5. A schematic diagram to show the possibility of domain merging. The neighboring sites (i, j) and $(i, j + 1)$ obtain different labels during the scan. In this case, the two domains need to be merged, and a single label is to be retained.

boundary are referred as the hull generating algorithms in the percolation theory [32,33]. To identify the boundary, we *march* along it in the clockwise direction, one bond at a time. For a domain, the starting site of the march (x_s, y_s) is identified as the leftmost site along one of the rows. Then the march is initiated after identifying the hop along the boundary to reach (x_s, y_s) . We refer to this as the *prior hop*.

A. Identifying the prior hop

The starting point (x_s, y_s) , as mentioned earlier, is the leftmost site of the domain along a row. Let the domain be labeled with m . Hence, there are only two possibilities of the prior hop through which it can reach the site. These are as shown in the Figs. 6(a) and 6(b). Thus, it is sufficient to check the label at the two lattice sites (x_{s+1}, y_s) and (x_s, y_{s-1}) . The one with label m defines the originating site of the prior hop. With this information we can initiate the march. At the later hops too, the determination of the next hop requires the identification of the previous hop and this information is at hand once the march begins.

B. Clockwise scan

After the identification of the prior hop, we scan the other three nearest neighbors of the site (x_s, y_s) to identify the next site on the boundary. The scanning is done in the clockwise direction with respect to the orientation of the prior hop. This is schematically shown in Figs. 6(c) and 6(d). The scan is terminated when we encounter a neighbor with label m . Let this neighbor be identified as $(x_{s'}, y_{s'})$ and it is the next site on the boundary. If all the three neighbors have label -1 , then the march proceeds by retracing along the prior hop and origin of

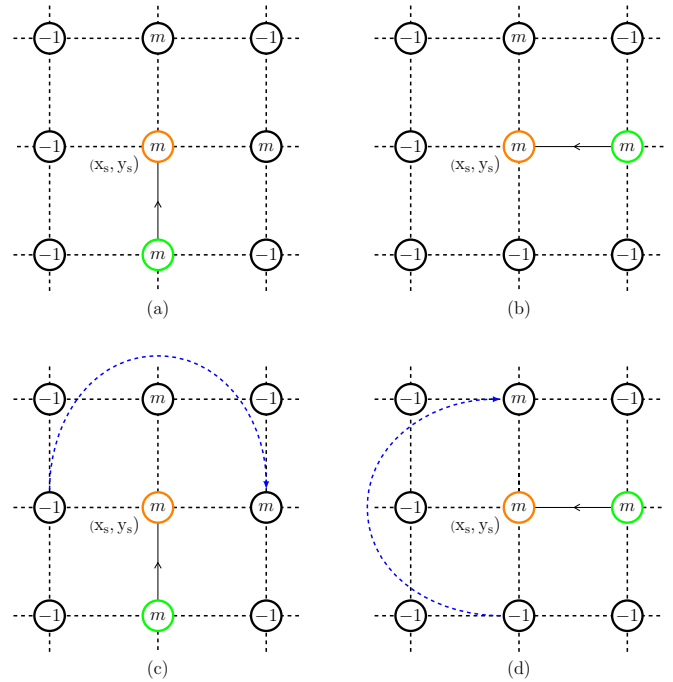


FIG. 6. A schematic diagram to illustrate the prior hop and the clockwise scanning for the boundary *march*. The march is started from the leftmost site (x_s, y_s) as highlighted by the peach color. The black arrow represents the prior hop to reach the site (x_s, y_s) . As illustrated in text, this prior hop can be either in upward direction [panel (a)] or leftward direction [panel (b)]. Panels (c) and (d), the blue dashed arrow indicates the scanning of the neighbors of (x_s, y_s) in a clockwise manner with respect to the orientation of the prior hop. The neighbor with label m first encountered in this clockwise scan then becomes next site on the boundary.

the prior hop is identified as the lattice site $(x'_{s'}, y'_{s'})$. The bond connecting the two lattice sites (x_s, y_s) and $(x'_{s'}, y'_{s'})$ defines the orientation of the prior hop to scan for the next lattice site on the boundary after $(x'_{s'}, y'_{s'})$. This process of scanning is repeated until we return to the starting site (x_s, y_s) .

As a representative case, we show the path along the boundary of a cluster in Fig. 7. The starting site (x_s, y_s) is the leftmost site of the bottom row and is highlighted in green color. The prior hop to reach (x_s, y_s) is leftward in this case and shown by a gray arrow. Once the starting site and the prior hop are identified, the scanning of nearest neighbors proceeds to identify the next site on the boundary. As explained, the march is completed when we return to the initial starting site (x_s, y_s) . An important prerequisite for the boundary march is thus the identification of the starting site and the prior hop.

V. COMPARISON OF THE ALGORITHM WITH OTHER METHODS

As mentioned in the Introduction, there are other well-known algorithms to identify domains in the percolation analysis. In this section, we compare the proposed algorithm with two of the standard algorithms; these are the HK and the recursive neighbor search algorithms. The comparisons are based on two parameters, the compute time and memory required. To get the general trends, the system size is varied

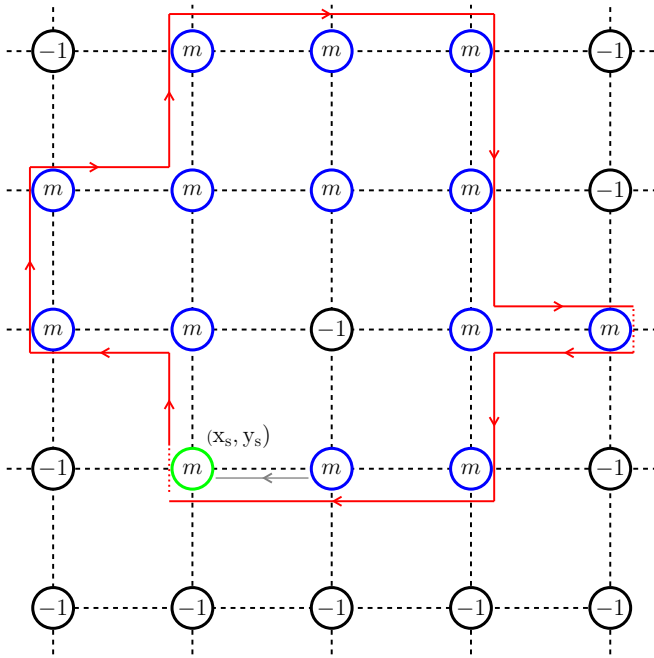


FIG. 7. A schematic illustration of the march along the boundary of a cluster of label m . The leftmost site (x_s, y_s) in the bottom row is the starting site of the march. The prior hop along the boundary to reach (x_s, y_s) is the site (x_{s+1}, y_s) , thereby this is leftward prior hop. This is shown by the gray colored arrow. The red arrows denote the directionality of the boundary march of the cluster shown in the figure.

over four orders of magnitude from 10^4 to 10^8 . And for each system size the runtime is taken as the average of 40 configurations. The configurations are generated using univariate random numbers generated using the Marsenne twister pseudorandom number generator.

A. Hoshen-Kopelman algorithm

It is a multiple cluster labeling algorithm widely used in clustering and percolation studies. In this algorithm, the lattice sites and their neighbors are scanned systematically, and the sites are labeled according to the occupancy. So in this method a cluster may comprise smaller clusters or subclusters with different labels. An equivalence class of the different labels of the subclusters identify a cluster. Thus, the HK algorithm constructs a coarse-grained linking between the cluster labels. On the contrary, the DC algorithm is fine-grained in character as it creates intersite links. Such a fine-grained approach may be better suited for the characterization and properties calculations using percolation theory. In the HK framework, additional lattice scan is required while computing cluster properties. However, in the DC algorithm, the linked-list identifies members of a cluster and traverse through the cluster with a unique path. Additional scans are not required. Thus, the DC algorithm is suitable for percolation problems that rely on identifying and analyzing the cluster properties.

Furthermore, an additional scan after the first lattice scan is required in the HK algorithm to label the clusters with a unique cluster label. This postprocessing step in the HK

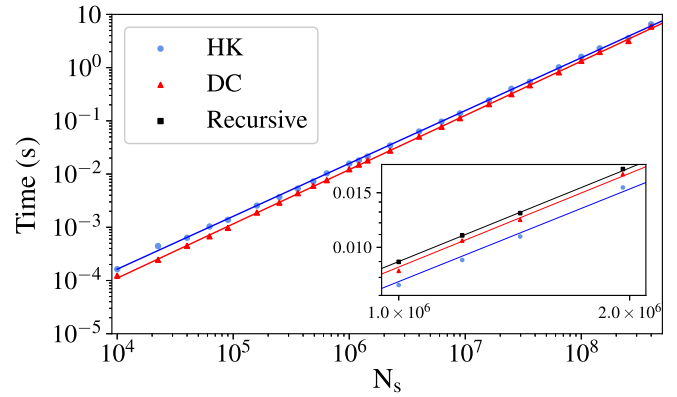


FIG. 8. The runtime of the HK (solid blue circles), the proposed DC algorithm (solid red triangles), and recursive neighbor search algorithms (solid black squares) for different lattice sizes N_s . The main panel shows total time required for the first scan and the postprocessing in the HK and the DC algorithms. For comparison of all the three methods, the inset plot shows the time required for the first scan in the three algorithms.

algorithm makes it slower than the DC algorithm, as shown in Fig. 8 (main panel). The details of the comparative studies related to the Fig. 8 are given in Appendix A.

The memory required in the DC algorithm is about three times larger than the HK algorithm. This is expected as the DC method needs memory to construct the linked lists. Considering the recent advances in memory hardware technology this is not a significant limitation. However, a decade ago, when very large memory configurations were not possible, it would have made a huge difference. In summary, the fine-grained linking of the DC algorithm offers an advantage and renders it suitable for the cluster characterization and properties calculations.

B. Recursive neighbor search algorithm

The recursive neighbor search algorithm involves scanning and labeling the neighbors of the occupied sites recursively. In this method, if an occupied site is found during the scan, then it is relabeled and the neighbors of this site are scanned. This process is continued recursively until all the sites of the cluster are identified. The method is implemented with relative ease using recursive function call. The key advantage of this approach is only the required cluster can be identified without the need to identify other clusters. However, as shown in the inset of Fig. 8 and discussed in Appendix A, this algorithm is slower than the DC and the HK algorithms. In addition, studies have shown that the number of the recursive functions becomes very large for larger system sizes [34]. This limitation does not apply to the DC algorithm as it is not based on recursion. Further, the recursive neighbor search is also not efficient for properties calculations as the domain information is not stored and each cluster characterization requires a lattice scan. It is to be noted that the problems studied in the percolation theory are not restricted to cluster identification and their characterizations. The choice of the numerical approach to study the percolation problems should therefore be based on the nature and complexity of the problem of interest.

VI. MI-SF QUENCH DYNAMICS

The MI phase to the SF phase quench dynamics of the Bose-Hubbard model [27], a model which describes the physics of ultracold bosons in optical lattices [35], has been experimentally realized [36]. During the quench, as the system crosses the critical point, SF domains are formed within MI as a background. We quantify the number of the SF domains using our domain counting algorithm. To discuss the dynamics, we first introduce the BHM Hamiltonian.

A. BHM Hamiltonian

The BHM Hamiltonian which describes the physics of ultracold bosonic atoms loaded in a 2D square optical lattice is [27,35]

$$\hat{H} = - \sum_{(i,j)} J(\hat{b}_i^\dagger \hat{b}_j + \text{H.c.}) + \sum_i \hat{n}_i \left[\frac{U}{2}(\hat{n}_i - 1) - \mu \right], \quad (2)$$

where $i \equiv (p, q)$ represent the lattice indexes, $j \equiv (p', q')$ are the indexes of its neighboring lattice site, \hat{b}_i^\dagger (\hat{b}_i) are the creation (annihilation) operators, \hat{n}_i is the bosonic occupation number operator, and the summation indexes within $\langle \dots \rangle$ denote the sum over the nearest neighbors. Further, J is the hopping strength, $U > 0$ is the on-site interatomic interaction strength, and μ is the chemical potential.

The incompressible MI state and the compressible SF state are the two ground states of the BHM Hamiltonian in the strongly interacting ($J/U \ll 1$) and weakly interacting ($J/U \gg 1$) domains, respectively [27,35]. The quantum phase transition between these two phases has been observed experimentally [37,38]. The MI state has integer commensurate lattice site occupancies, and the bosons are pinned to the lattice sites. The SF state, on the other hand, features a real valued occupancy, and it is a conducting phase. The two phases are identified based on the SF order parameter

$$\phi_{p,q} = \langle \hat{b}_{p,q} \rangle. \quad (3)$$

It is zero in the MI phase and nonzero in the SF phase. For a homogeneous lattice system, $\phi_{p,q}$ is uniform throughout the lattice. For our studies, we use the single-site Gutzwiller mean-field (SGMF) method to obtain the ground state of the model and phase diagram. In this method, the annihilation (creation) operators in Eq. (2) are separated into a mean-field ϕ (ϕ^*) and a fluctuation operator [39,40]. The Hamiltonian in Eq. (2) can then be approximated as the mean-field Hamiltonian which is a sum of single site Hamiltonians $\hat{H}_{\text{MF}} = \sum_{p,q} \hat{h}_{p,q}$. We perform self-consistent calculation of $\phi_{p,q}$ until the desired convergence is obtained. The details of using this method in our computations are given in our previous works [30,41–46].

B. Quench dynamics

To study the MI-SF quench dynamics of the system, the hopping amplitude J is ramped from an initial value J_i to a final value J_f . These are chosen such that J_i and J_f correspond to the MI and SF phases, respectively. The remaining parameters of the system are held fixed. Then the temporal evolution of the system during the quench and afterwards is described

by the time-dependent Schrödinger equation,

$$i\hbar \partial_t |\psi\rangle_{p,q} = \hat{h}_{p,q} |\psi\rangle_{p,q}, \quad (4)$$

where $|\psi\rangle_{p,q}$ is the wave function at site (p, q) . Due to the intersite coupling through the order parameter ϕ , we obtain a set of coupled partial differential equations. These are solved using the fourth-order Runge-Kutta method. To start the quench, we obtain the equilibrium wave function with the $J = J_i$ and introduce phase and density fluctuations to it [46]. These fluctuations simulate the quantum fluctuations essential to drive the quantum phase transition. To calculate system properties we take the ensemble average of a set consisting of 80 such randomized initial states.

We examine the nonequilibrium dynamics of the system during the quench from the KZM perspective. It categorizes the quench dynamics into three temporal regimes [47,48], corresponding to the adiabatic, impulse, and adiabatic regime. These temporal regimes arise due to the critical slowing down near the quantum critical point (QCP). It predicts the rate of the topological defects formation during the course of the quench dynamics [18–22]. These defects are generated at the meeting points of the domains of the symmetry broken phase. This is due to the local gauge choices of the order parameter associated with the domains. For point defects like vortices, the density of defects is hence proportional to the number of domains. It is to be mentioned that the transition from MI to SF phase breaks the global $U(1)$ symmetry spontaneously. Then number of the domains N_D satisfies the scaling law

$$N_D \propto \tau_Q^{-d}, \quad (5)$$

where $1/\tau_Q$ is the quench rate and exponent $d = 2\nu/(1 + \nu z)$. Here ν is the critical exponent of the equilibrium correlation length and z is the dynamical critical exponent. It is to be noted that these scaling laws are applicable at \hat{t} , which is the time at which the system transits from the impulse to the adiabatic domain. The details of locating \hat{t} are given in our previous work [46]. The same scaling law is also applicable to the defect density N_v . For the MI-SF transition the defects are the vortices and their density is given by [23–25,46]

$$N_v = \sum_{p,q} |\Omega_{p,q}|, \quad (6)$$

with

$$\Omega_{p,q} = \frac{1}{4} [\sin(\theta_{p+1,q} - \theta_{p,q}) + \sin(\theta_{p+1,q+1} - \theta_{p+1,q}) - \sin(\theta_{p+1,q+1} - \theta_{p,q+1}) - \sin(\theta_{p,q+1} - \theta_{p,q})], \quad (7)$$

where $\theta_{p,q}$ is the phase of $\phi_{p,q}$. In the results section, we first calculate the critical exponent d from the defect density N_v . Then we use our method to calculate N_D and show that we get similar value of the critical exponent based on N_D . This serves as an excellent cross checking of two different approaches to estimate the same critical exponent.

C. Results

To study the MI-SF nonequilibrium quench dynamics, we consider a system of size of 100×100 . The Hamiltonian is scaled with U and time is defined in the units of \hbar/U . The hopping amplitude J is evolved using the following quench

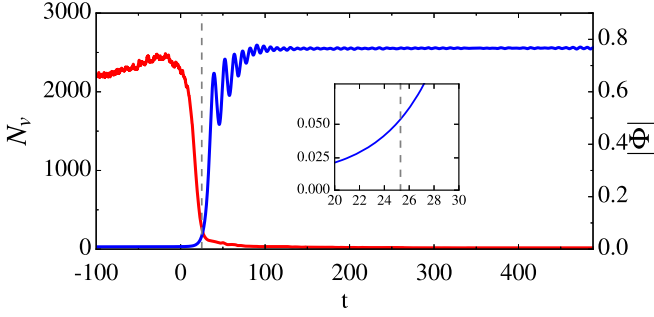


FIG. 9. The time evolution of the vortex density N_v (red) and $|\Phi|$ (blue) as a function of time, for $\tau_Q = 100$. The QCP is crossed at $t = 0$, and the dashed gray line indicates the time \hat{t} . The order parameter $|\Phi|$ rises exponentially after \hat{t} , as shown in the inset. The vortex density N_v exhibits a steep decrease after crossing the QCP due to the annihilation of the vortex-antivortex pairs.

protocol:

$$J(t) = J_i + \frac{(J_c - J_i)}{\tau_Q}(t + \tau_Q). \quad (8)$$

With this protocol, we have $J(-\tau_Q) = J_i$ and $J(0) = J_c$ is the QCP of the MI-SF phase transition. For our study we take $J_i = 0.0U$ and $J_f = 0.08U$ and fix the chemical potential $\mu = 0.41U$. The value of the μ is chosen so that it corresponds to the tip of the MI(1) lobe and $J_c = 0.042U$. Thus, at $t = -\tau_Q$, the system is in the MI(1) phase, and at $t = t_f$, it is in the SF phase when the quantum quench ends.

1. Transition from MI to SF phase

As an indicator of the quench dynamics, the temporal evolution of $|\Phi| = \sum_{p,q} |\phi_{p,q}|/N_s$ and N_v during the quench, for $\tau_Q = 100$ are shown in Fig. 9. Here N_s denotes the number of lattice sites. In the initial stages of the quench dynamics, $|\Phi|$ is close to zero ($\sim 10^{-3}$) and remains so until \hat{t} . In the equilibrium MI state, $|\Phi|$ is zero, but in the quench dynamics it is finite due to the fluctuations added in the initial-state preparation. As the QCP is crossed at $t = 0$, the system ought to evolve into SF phase ($t > 0$) and acquire a larger $|\Phi|$. But, as the system is still in the impulse domain, the $|\Phi|$ remains small until it ends at \hat{t} . Post \hat{t} , there is an exponential increase of $|\Phi|$, which is discernible from the plot in Fig. 9. After the exponential increase, the $|\Phi|$ settles to a steady-state value.

The snapshots of $|\phi_{p,q}|$ at different times are shown in Fig. 10. The small values of $|\phi_{p,q}|$ at initial time $t = -\tau_Q$ is as shown in Fig. 10(a). The figure also indicates the fluctuations present in the values of $|\phi_{p,q}|$. The Fig. 10(b) shows the formation SF domains at \hat{t} when the system re-enter the adiabatic domain. The domains can be easily counted using our method. When J/U is further increased, these domains grow in size, and merge through the phase ordering process. This is visible from the Figs. 10(c) and 10(d), in these figures $|\phi_{p,q}|$ is almost uniform.

The evolution of defect density N_v is complimentary to that of $|\Phi|$. At the initial stages of the quench, N_v is high (≈ 2200), this is due to the large phase fluctuations added to the initial state. It decrease after the system crosses QCP. This happens as the SF domains begin to form and phase coherence within

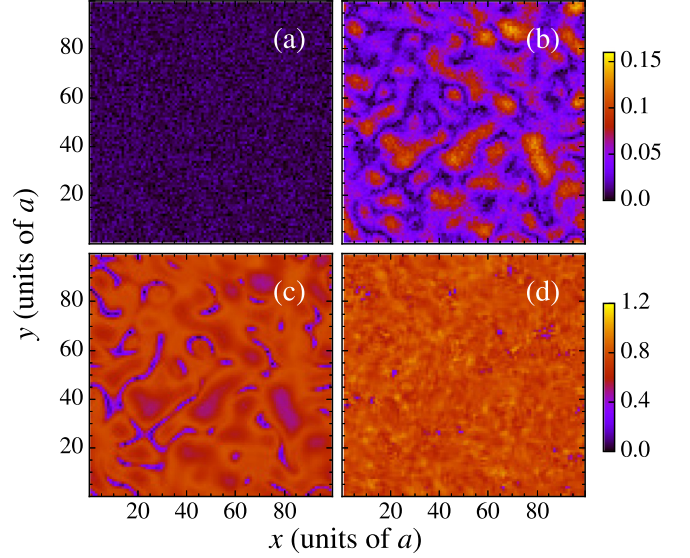


FIG. 10. Snapshots of $|\phi_{p,q}|$ at certain time instants for $\tau_Q = 100$. At initial time $t = -\tau_Q$, $|\phi_{p,q}|$ is small as shown in (a). After \hat{t} , the $|\phi_{p,q}|$ increases and domains of SF are formed. This is shown in panel (b) which is at $t = \hat{t}$. These domains disappear due to the merging as time progresses and the system becomes homogeneous, as shown in panels (c) and (d).

the domains prevent the presence of a vortex inside a domain. As time progresses, the phase ordering takes places, and these domains merge. The domain merger results in the annihilation of the vortex-antivortex pairs, further reducing N_v . This is discernible from Fig. 9.

2. Critical exponents and scaling laws

To study the scaling of the N_v with τ_Q , we compute N_v over a range of τ_Q . As mentioned earlier, the scaling laws are considered at time \hat{t} . Hence, we compute N_v at \hat{t} for every τ_Q . The log-log plot of the values obtained are shown in Fig. 11(a). From least-squares fitting, we get the value of the critical exponent d as 0.41. That is, $N_v \propto \tau_Q^{-0.41}$.

Following similar analysis, we determine the scaling exponent of the N_D with the quench rate. As shown in Fig. 10(b), SF domains begins to appear at \hat{t} . These domains are characterized by a finite value of the SF order parameter. Since the MI regions also have a small nonzero SF order parameter, owing to the initial fluctuations, we set a threshold ϵ of the $|\phi_{p,q}|$ to distinguish the SF phase from the MI phase. The value of ϵ is taken as the average of $|\phi_{p,q}|$ over the prominent MI phase regions in the system at $t = 0$. In our computations, based on this definition, we get $\epsilon \approx 0.07$. We then calculate the ensemble-averaged value of N_D using our method. From the results, the scaling of N_D with τ_Q is as shown in Fig. 11(b). We observe a power-law scaling,

$$N_D \propto \tau_Q^{-0.39}, \quad (9)$$

that is, the critical exponent $d = 0.39$. This implies that the scaling of the N_D with τ_Q is approximately same as the scaling of the N_v with τ_Q . This is expected from the KZM, as the density of the topological vortices is used as a proxy for the number of domains. Thus, the domain counting algorithm

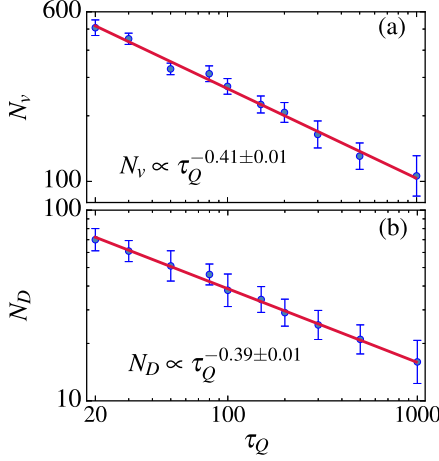


FIG. 11. Scaling of the vortex density N_v and number of domains N_D , with respect to τ_Q . From (a), we see that the exponent $d = 0.41$. The scaling exponent for N_D versus τ_Q is 0.39, as shown in (b). The blue error bars represent the standard deviation of the data values.

predicts an exponent that is in a good agreement with the exponent obtained from the vortex density. Here it is to be noted that the methods used in computing N_D and N_v are different. One is based on the current distribution and our method is based on the identification of clusters. The two in essence serve as independent checks of the KZM scaling of the MI-SF transition.

VII. DISORDERED BOSE-HUBBARD MODEL

The analysis of the MI-SF quench dynamics utilized the domain counting aspect of the method we have developed. The fine-grained nature of the method also makes it suitable for detailed analysis of the clusters as well. We apply this to study the critical properties of the BG to SF transition in the 2D square optical lattice with disorder. The system is modeled with the disordered Bose-Hubbard model (DBHM). Earlier studies have identified the ground-state phase diagram of the DBHM and have shown the absence of a direct MI-to-SF transition [27–30,49–51]. The MI-SF transition is intervened by the BG phase, which is characterized by nonzero compressibility and zero superfluid stiffness. Structurally, this is essentially the MI phase inlaid with SF islands and the SF islands lead to the finite compressibility. However, the superfluid stiffness is zero as the islands cannot generate phase coherence across the system. Thus, in terms of percolation theory, the SF islands in the BG phase are nonpercolating. But, the clusters percolate when the BG phase undergoes a transition to the SF phase. Therefore, the BG-to-SF transition can be viewed as the percolation analysis of the SF clusters. Previous works [52–54] have studied the geometric properties of the SF clusters and compared the onset of superfluidity with the percolating transition of the system. In this work, we delve into the cluster properties using our method. In particular, we study the power-law divergence of the correlation length of the system near the percolating transition and extract the critical exponent ν quantifying the divergence. We also compute the fractal dimension of the hulls of the SF clusters using the boundary walk algorithm discussed earlier. These studies re-

veal that the BG-to-SF transition falls in the universality class of 2D random percolation.

A. DBHM Hamiltonian

The DBHM Hamiltonian of the 2D square optical lattice is [27,30,52]

$$\hat{H} = - \sum_{\langle i,j \rangle} J(\hat{b}_i^\dagger \hat{b}_j + \text{H.c.}) + \sum_i \hat{n}_i \left[\frac{U}{2}(\hat{n}_i - 1) - \tilde{\mu}_i \right], \quad (10)$$

where, except for $\tilde{\mu}_i$, the model parameters have the same meaning as the BHM Hamiltonian in Eq. (2). Here the effective chemical potential $\tilde{\mu}_i = \mu - \epsilon_i$ is site dependent, and $\epsilon_i \in [-\Delta, \Delta]$ is a univariate random number to simulate diagonal disorder. The parameter Δ denotes the strength of the disorder. In the experiments, the disordered lattice potential is generated by shining a speckle beam [55–57].

The ground-state phase diagram of the DBHM exhibits the quantum phases determined by the competition between the hopping energy J , the interaction energy U , and the disorder strength Δ . Then, like in the BHM, we use the SGMF method to obtain the quantum phases and their characteristic order parameters. For a moderate Δ , when J/U is small, the strong onsite repulsion favors the incompressible MI phase and atoms are pinned to the sites. For large J/U , the large hopping strength favors the compressible SF phase and atoms are itinerant. In the intermediate J/U the two phases are separated by the BG phase. As mentioned earlier, the BG phase is characterized by SF islands in the background sea of insulating MI phase. These islands impart finite number fluctuations $\delta n_{p,q}$ to the BG phase. Hence, $\delta n_{p,q}$ is an order parameter to distinguish the BG phase from the number coherent MI phase. For the site (p, q) ,

$$\delta n_{p,q} = \sqrt{\langle \hat{n}_{p,q}^2 \rangle - \langle \hat{n}_{p,q} \rangle^2}, \quad (11)$$

where the expectation value $\langle \dots \rangle$ is taken with respect to the ground state. At the BG-SF phase boundary, the SF stiffness ρ_s is the relevant order parameter to differentiate the BG and SF phases. It denotes the finite energy required to alter the phase of the wave function of the system. Since the SF phase is phase coherent, it exhibits a stiffness or resistance for the phase change. So, ρ_s is nonzero in the SF phase. But, it is zero in the MI phase and nonzero but small in the BG phase. To compute ρ_s , we impose twisted boundary condition. It modifies the hopping terms by introducing Peierls phase factors [58–61]. For the DBHM, we impose twisted boundary condition along the x direction and transform the hopping terms as [59,61]

$$J(\hat{b}_{p+1,q}^\dagger \hat{b}_{p,q} + \text{H.c.}) \rightarrow J(\hat{b}_{p+1,q}^\dagger \hat{b}_{p,q} e^{i2\pi\varphi/L_x} + \text{H.c.}). \quad (12)$$

The SF stiffness is then defined as

$$\rho_s = \frac{L_x}{8\pi^2} \left. \frac{\partial^2 E_0}{\partial \varphi^2} \right|_{\varphi=0}, \quad (13)$$

where E_0 is the ground-state energy with twisted boundary condition.

For our studies based on the statistics of the SF clusters in the BG phase, we choose the system size as 1000×1000 . The order parameters $\delta n_{p,q}$ and ρ_s are taken as ensemble average of 60 disorder realizations. Here it is to be added that we observe finite-size effects for system sizes up to 100×100 . We attribute this to the poor statistics as a result of fewer domains in a smaller system size. The remedy is to increase the number of domains by increasing the system size and improve the statistics. This reduces the sample to sample variation in the quantities like the correlation length. The system size of 100×100 is, however, suitable for other studies to probe properties which depend on the average or coarse grained measures like the determination of the phase diagram and quench dynamics.

B. Percolation analysis

The percolation theory analyzes the statistical and geometrical properties of the clusters of sites on a lattice [4]. Specifically, in the site-percolation problem, every lattice site is independently and randomly occupied with probability p . The collection of neighboring occupied sites is termed as a cluster. For small p , a majority of the clusters constitute small number of sites and are isolated, while for large p , a majority of the occupied sites form a percolating cluster which spans from one edge to the opposite edge. Thus, there exists a critical threshold probability p_c so that for $p < p_c$, there is no spanning cluster, and for $p \geq p_c$, there exists at least one spanning cluster. Such a percolating transition is characterized by power-law divergences and universal critical exponents. One property which exhibits divergence at transition is the correlation length of the system ξ . It can be defined as an average over the cluster radii in the system

$$\xi^2 = \frac{\sum_s R_s^2 s^2 n_s}{\sum_s s^2 n_s}, \quad (14)$$

where R_s is the gyration radius of the cluster of s sites and the n_s denotes the average number of clusters of size s per site. In the summation, the contribution from the infinite, percolating clusters is omitted [4,5]. At the percolation transition ξ shows power-law divergence,

$$\xi \propto |p - p_c|^{-\nu}. \quad (15)$$

The calculation of R_s involves the evaluation of the distance of a lattice site from the center of mass of the cluster [4,5]. For systems with the periodic boundary conditions (PBC), due to the absence of edges, there are two possible definitions of the distance between two lattice sites. To resolve this in a consistent way, we unwrap the system. So that the clusters in the original system are mapped onto a system where dimensions are doubled. In the larger system, the distance between the lattice sites in a cluster are defined without ambiguity. The details of this procedure are given in the Appendix B.

In the BG phase, the sites with nonzero SF order parameter are considered as occupied sites. Hence, as the critical J_c of the BG-to-SF transition is approached, we expect the SF clusters to percolate. So, we can equivalently write the power-law divergence in terms of reduced hopping strength as

$$\xi \propto |J - J_c|^{-\nu}. \quad (16)$$

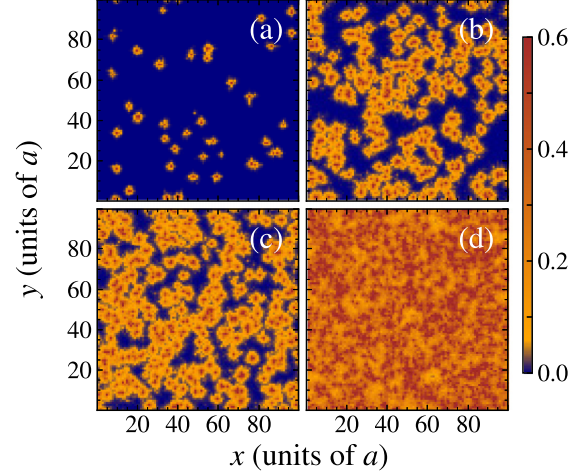


FIG. 12. Snapshots of $|\phi_{p,q}|$ at different J/U values. Panels (a)–(d) correspond to the J/U values as 0.009, 0.017, 0.019, and 0.025 respectively. As the J/U is increased, the SF domains percolate and the system undergoes a transition from the BG to SF phase. The chosen parameters are $\mu = 0.2U$ and $\Delta = 1.2U$. Panel (b) illustrates the order parameter profile just before the percolation transition.

To identify the occupied sites we choose a threshold of 10^{-3} for the SF order parameter.

C. Results of BG-to-SF transition

For the percolation analysis we take $\Delta = 1.2U$ and $\mu = 0.2U$ and scan the phases as a function of J/U . The phase diagram in the $J/U - \mu/U$ plane, as reported in Ref. [30], constitutes the BG and SF phases. The absence of the MI phase is due to the high disorder strength. The snapshots of $|\phi_{p,q}|$ for selected values of J/U are shown in Fig. 12, for a 100×100 system and $\mu/U = 0.2$. In the figure the rare SF islands in the BG phase are visible in the Fig. 12(a) for $J/U = 0.009$. These SF islands are nonpercolating, and hence the introduction of a phase twist does not cost energy. The SF islands increase in size as J/U is increased; this is evident in Fig. 12(b), which shows $|\phi_{p,q}|$ for $J/U = 0.017$. This snapshot illustrates the order parameter profile before the percolation transition and highlights the large SF islands in the system. Although the SF islands are large, there is no spanning cluster. On reaching critical J/U a spanning cluster emerges and system undergoes percolation transition. This is illustrated in the Fig. 12(c), the system supports a spanning cluster for $J/U = 0.019$. Due to the spanning SF cluster, introducing a phase twist costs energy and superfluid stiffness ρ_s assumes a finite value. On further increase of J/U the background MI phase region is completely depleted and the entire system is in the SF phase. This is discernible from the Fig. 12(d).

In the Fig. 13(a), the correlation length ξ is shown as a function of J/U . As evident from the figure ξ diverges near $J/U \approx 0.017$ and this signals a percolation transition from the BG phase to the SF phase. Using the relation in Eq. (16) we can calculate the exponent ν which quantifies the divergence

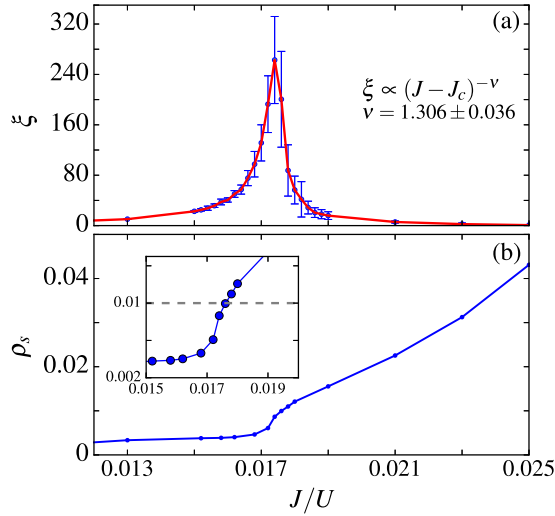


FIG. 13. Plot of the correlation length ξ and the superfluid stiffness ρ_s as a function of J/U . The chemical potential is $\mu = 0.2U$ and disorder strength is $\Delta = 1.2U$ for these calculations. The results are obtained by averaging over 60 disorder realizations. In (a), we observe a divergence of ξ , signaling the percolation transition from the BG to SF phase, with J_c near $0.017U$. The critical exponent is $\nu = 1.306 \pm 0.036$. The standard deviation from the average value is shown by the blue error bar. Panel (b) illustrates the stiffness ρ_s as a function of J/U . There is an increase in the stiffness near $J/U \approx 0.017$ as shown in the inset. For numerical calculations, the threshold value 0.01 (shown in gray dashed line) is considered to distinguish between the BG and SF phase.

and obtain $\nu = 1.306 \pm 0.036$. This is in excellent agreement with the value $\nu = 4/3$ corresponding to the universality class of 2D random percolation model. Previous studies [52,62] have also computed the exponent ν and the values reported are in good agreement with our results. To study the BG-to-SF transition further, we plot ρ_s as a function of J/U in Fig. 13(b). The calculation of ρ_s are performed with a 100×100 system, as the computations with the twisted boundary conditions are compute intensive and require long execution times for a 1000×1000 system. As mentioned earlier, ρ_s is small in the BG phase owing to the absence of a global phase coherence in the system. It shows an increase as the system enters the SF domain. Based on our previous work [30], we consider $\rho_s \approx 10^{-2}$ as a threshold for distinguishing between the BG and SF phase. The plot shows an increase in ρ_s at $J/U \approx 0.017$, and the threshold is crossed at $J = 0.0174U$. This is also the point where ξ shows divergence. Thus, the identification of the BG-SF transition with the order parameter ρ_s matches with the percolation analysis. Given the fine-grained approach of our method, the properties of the domain formation and their dynamical evolution can be analyzed using our method. This shall be addressed in our future works.

D. Fractal dimension of hulls of SF clusters

The percolating clusters near the percolation transition are self-similar and can be characterized by a fractal dimension. In particular, the perimeter of the clusters close to the

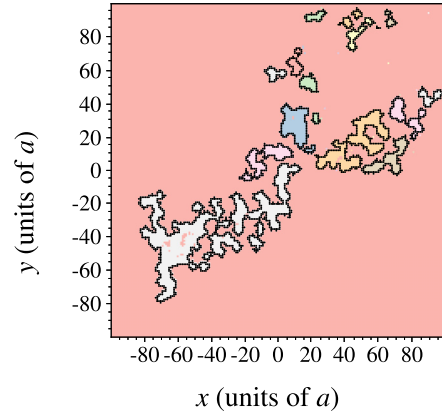


FIG. 14. Charted boundary of the SF clusters shown in Fig. 12(b) after unwrapping the system. The clusters in the original system are mapped onto the system with double dimensions. The SF clusters are identified with different colors in the figure.

percolation transition point is similar to a random walk with many fractured edges and can be characterized by a fractal dimension D which can be computed using the area-perimeter relation

$$H \propto A^{D/2}, \quad (17)$$

where H is the perimeter or the hull and A is the area of the cluster. In this subsection, we investigate the fractal properties and the compute the fractal dimension of the SF islands close to the BG-SF transition point.

For our studies, we consider $J = 0.017U$ for a 100×100 system and consider 60 disorder realizations. Once we identify the equilibrium configurations of each of these 60 realizations and identify the SF islands, we use the boundary walk algorithm to compute the hulls of the clusters. As J is close to criticality, there are clusters which lie across the edges along the x and y directions due to the periodic boundary conditions. To simplify the analysis, we unwrapped the system and mapped the clusters onto a larger system. This ensures that each cluster forms an island without touching the edges. Then, the starting site and the prior hop for the boundary walk can be accomplished without any ambiguity. As an illustration, we show the unwrapping of the order parameter profile corresponding to Fig. 12(b) and the charted boundaries of these clusters in Fig. 14. The hull of all the clusters in other disorder realizations are computed in same way. The variation in the hull of these clusters with the cluster area is shown in Fig. 15. In this plot, the hulls of clusters with area in the bin $[A, A + \delta A]$ are averaged to give $H(A)$. We have chosen $\delta A = 0.3A$ for our studies. The $\delta A \propto A$ assures uniform spacing in the $\log A$ scale. We do a least-squares fit to the data using the area-perimeter scaling given in Eq. (17) and the result is shown in Fig. 15. The fractal dimension D obtained from the results is 1.72 ± 0.02 . This value is in good agreement with the predicted value of the fractal dimension $D = 1.75$ in the universality class of 2D random percolation [33,63,64,65]. Thus the analysis of the fractal dimension of the SF islands in the BG phase complements or confirms the earlier conclusion that the BG-SF transition belongs to

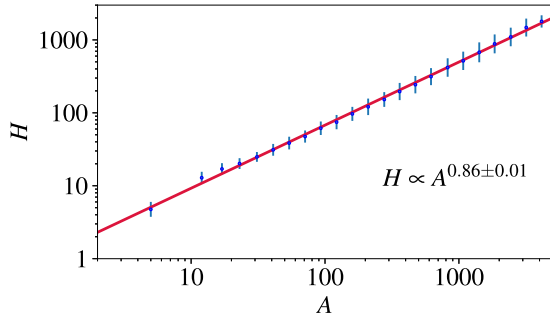


FIG. 15. Power-law scaling of the hulls of the clusters with their area. The data points are represented by blue color, while the red line is the best fit to the data. The fractal dimension from this analysis is $D = 1.72$.

the universality class of 2D random percolation. This is one example application of the fine-grained analysis using the DC algorithm.

VIII. CONCLUSION

To summarize, we have developed an algorithm to identify clusters or domains and study their percolation properties on a 2D lattice. The algorithm exploits the structure of the linked-lists data type and enumerates the clusters on the lattice with a single scan. Further, the locations of the sites constituting a cluster are stored, and this facilitates the application of methods based on percolation theory. Our approach, with minor modifications in the scanning process, can be adapted to lattices of higher dimensions. Based on the results, we also present an algorithm to identify the boundary of the cluster. Using the algorithm, we compute the number of domains formed in the MI-SF quench dynamics and calculate the critical exponent. The critical exponent so obtained is in excellent agreement with the result from the vortex density. Further, we also study the BG-SF transition in the DBHM. For this we calculate the correlation length of the SF clusters and observe a divergence near the BG-SF transition. In addition, we have computed the fractal dimension of the SF clusters near the BG-SF transition. The exponent ν associated with the divergence of correlation length and the fractal dimension D suggests that the BG-SF transition belongs to the universality class of 2D random percolation.

ACKNOWLEDGMENTS

The results presented in the paper are based on the computations using Vikram-100, the 100TFLOP HPC Cluster at Physical Research Laboratory, Ahmedabad, India. D.A. acknowledges support from the Science and Engineering Research Board, Department of Science and Technology, Government of India, through Project No. CRG/2022/007099 and support from the UGC through the SAP (DRS-II) Project No. F.530/18/DRS-II/2018(SAP-I), Department of Physics, Manipur University. The authors are grateful to Dr. Sukla Pal, Dr. Kuldeep Suthar, Dr. Rukmani Bai, and Dr. Soumik Bandyopadhyay for the fruitful discussions and their comments to improve the paper.

APPENDIX A: COMPARISON WITH OTHER ALGORITHMS

We have compared the execution times for the domain identification required by the HK, DC, and the recursive neighbor search algorithms. The comparison is based on analysis of randomly generated 40 lattice configurations. In each member the sites are randomly labeled with 0 and -1 . As mentioned earlier, the sites labeled 0 are to be identified as a domain. For comparison, for each member the execution time using the three algorithms are noted. To remove the effects of fluctuation on account of system load and other factors, an average of the results is calculated from the 40 members. For uniformity and to avoid computational overheads, the FORTRAN implementation of these algorithms are executed on a HP EliteDesk PC with Intel i7 processor.

The comparison between the execution times of the HK and the DC algorithms are shown in Fig. 8. For the HK algorithm we have used the FORTRAN implementation by Anders from the GitHub [66]. The results indicate that the DC algorithm is marginally faster than the HK algorithm. The least-squares fit of the data gives $T_{DC} = 9.58N_s^{1.01}$ nanoseconds and $T_{HK} = 16.05N_s^{1.00}$ nanoseconds, where $T_{DC}(T_{HK})$ denote the execution time required in the DC (HK) algorithm. This suggests that both these methods have number of floating point operations proportional to the number of sites. However, it is to be noted that the execution time of the DC algorithm also includes the construction of the linked lists, and these lists can be utilized for further studies. The main panel in Fig. 8 includes time required for the first scan and the following postprocessing steps. In the DC algorithm, the postprocessing step is to reassign the cluster labels in ascending order, as the cluster labels after the first scan are not in a sequence. This step is thus to make the labels systematic which helps for percolation studies. However, post the first scan, the clusters are identified with unique labels thus completing the domain identification process. On the contrary, the second scan in the HK algorithm is necessary to label the clusters with unique labels. This further adds to the advantages of the DC algorithm.

The domain mergers are the reason for the postprocessing required in the DC and HK algorithms. However, there are no domain mergers in the recursion method, and hence there is no postprocessing of labels. Therefore we have compared the run time of the algorithms until the first scan, avoiding the postprocessing of the data, and the results are shown in the inset in Fig. 8. We have illustrated the comparison for a small range of lattice sizes for the readability of the figure. We notice that the DC algorithm requires extra time, around 4% more relative to the HK algorithm. This is due to the construction of the linked-lists. This also suggests that the postprocessing in the DC algorithm requires lesser time than that in the HK algorithm. This is to be expected, as in the DC algorithm, the postprocessing involves transfer of the linked-lists from the old to new cluster labels, without involving a second scan. However, for the HK algorithm, the postprocessing is the secondary lattice scan. It is also evident that the recursive neighbor search is slower than the DC and the HK algorithm, which is another disadvantage of this method.

APPENDIX B: SYSTEM UNWRAPPING

We describe the unwrapping procedure employed on the system required to compute the distances within the system. The aim is to map the system of size $L_x \times L_y$ with periodic boundary conditions onto a larger system of size $2L_x \times 2L_y$ with open boundary condition. To begin with, we first identify the clusters on the boundary of the system. For illustration, consider a cluster that straddles across the left and right edge of the system. Due to the PBC, the left and right chunks are a part of same cluster. The chunk of this cluster connected with the right edge of the system needs a x shift. The x shift implies that the chunk is translated along the negative x direction by distance L_x . After this step, the two chunks appear side by side and the distance between any two points is unique. Similarly

a y shift is assigned to a chunk of the cluster which straddles along bottom and top edge. In some cases, a cluster may straddle across both directions. In this case, certain chunks may require both x shift and y shift. As discussed in the main text, the unwrapping of the domain configuration of Fig. 12(b) is shown in Fig. 14. After these steps are performed, we compute the geometrical properties of the clusters. Here we mention that these steps are not valid for percolating clusters as they may be infinite in length and would not accommodate in a new system of finite size. But as stated in the main text, the percolation analysis of the system generally ignores the contribution from the percolating clusters, thereby shifting of the finite sized nonpercolating clusters suffices to perform the percolation studies.

-
- [1] S. R. Broadbent and J. M. Hammersley, Percolation processes: I. crystals and mazes, *Math. Proc. Camb. Philos. Soc.* **53**, 629 (1957).
- [2] R. J. Elliott, B. R. Heap, D. J. Morgan, and G. S. Rushbrooke, Equivalence of the critical concentrations in the Ising and Heisenberg models of ferromagnetism, *Phys. Rev. Lett.* **5**, 366 (1960).
- [3] P. J. Flory, *Principles of Polymer Chemistry* (Cornell University Press, New York, 1953).
- [4] D. Stauffer and A. Aharony, *Introduction To Percolation Theory* (Taylor & Francis, London, 1992).
- [5] Muhammad Sahimi and A. G. Hunt, *Complex Media and Percolation Theory* (Springer, New York, 2021).
- [6] J. Hoshen and R. Kopelman, Percolation and cluster distribution. I. Cluster multiple labeling technique and critical concentration algorithm, *Phys. Rev. B* **14**, 3438 (1976).
- [7] R. G. Moreira and M. A. Barrufet, Spatial distribution of oil after deep-fat frying of tortilla chips from a stochastic model, *J. Food Eng.* **27**, 279 (1996).
- [8] L. Zhang and N. A. Seaton, Simulation of catalyst fouling at the particle and reactor levels, *Chem. Eng. Sci.* **51**, 3257 (1996).
- [9] M. Berry, J. Comiskey, and K. Minser, Parallel analysis of clusters in landscape ecology, *IEEE Comput. Sci. Eng.* **1**, 24 (1994).
- [10] F. Eddi, J. Mariani, and G. Waysand, Transient synaptic redundancy in the developing cerebellum and isostatic random stacking of hard spheres, *Biol. Cybern.* **74**, 139 (1996).
- [11] J. Hoshen, M. W. Berry, and K. S. Minser, Percolation and cluster structure parameters: The enhanced Hoshen-Kopelman algorithm, *Phys. Rev. E* **56**, 1455 (1997).
- [12] S. Frijters, T. Krüger, and J. Harting, Parallelised Hoshen-Kopelman algorithm for lattice-Boltzmann simulations, *Comput. Phys. Commun.* **189**, 92 (2015).
- [13] J. M. Constantin, M. W. Berry, and B. T. V. Zanden, Parallelization of the Hoshen-Kopelman algorithm using a finite state machine, *Int. J. Supercomput. Appl. High Perf. Compu.* **11**, 34 (1997).
- [14] N. R. Moloney and G. Pruessner, Asynchronously parallelized percolation on distributed machines, *Phys. Rev. E* **67**, 037701 (2003).
- [15] J. M. Teuler and J. C. Gimel, A direct parallel implementation of the Hoshen-Kopelman algorithm for distributed memory architectures, *Comput. Phys. Commun.* **130**, 118 (2000).
- [16] N. Sendra, T. Gwizdała, and J. Czerbniak, Reducing algorithm for percolation cluster analysis, *Ann. UMCS Informatica* **5**, 87 (2006).
- [17] M. E. J. Newman and R. M. Ziff, Efficient Monte Carlo algorithm and high-precision results for percolation, *Phys. Rev. Lett.* **85**, 4104 (2000).
- [18] T. W. B. Kibble, Topology of cosmic domains and strings, *J. Phys. A: Math. Gen.* **9**, 1387 (1976).
- [19] T. W. B. Kibble, Some implications of a cosmological phase transition, *Phys. Rep.* **67**, 183 (1980).
- [20] W. H. Zurek, Cosmological experiments in superfluid helium? *Nature (London)* **317**, 505 (1985).
- [21] W. H. Zurek, Cosmological experiments in condensed matter systems, *Phys. Rep.* **276**, 177 (1996).
- [22] Adolfo del Campo and W. H. Zurek, Universality of phase transition dynamics: Topological defects from symmetry breaking, *Int. J. Mod. Phys. A* **29**, 1430018 (2014).
- [23] K. Shimizu, Y. Kuno, T. Hirano, and I. Ichinose, Dynamics of a quantum phase transition in the Bose-Hubbard model: Kibble-Zurek mechanism and beyond, *Phys. Rev. A* **97**, 033626 (2018).
- [24] K. Shimizu, T. Hirano, J. Park, Y. Kuno, and I. Ichinose, Out-of-equilibrium dynamics of multiple second-order quantum phase transitions in an extended Bose-Hubbard model: Superfluid, supersolid, and density wave, *Phys. Rev. A* **98**, 063603 (2018).
- [25] K. Shimizu, T. Hirano, J. Park, Y. Kuno, and I. Ichinose, Dynamics of first-order quantum phase transitions in extended Bose-Hubbard model: From density wave to superfluid and vice versa, *New J. Phys.* **20**, 083006 (2018).
- [26] Y. Zhou, Y. Li, R. Nath, and W. Li, Quench dynamics of Rydberg-dressed bosons on two-dimensional square lattices, *Phys. Rev. A* **101**, 013427 (2020).
- [27] M. P. A. Fisher, P. B. Weichman, G. Grinstein, and D. S. Fisher, Boson localization and the superfluid-insulator transition, *Phys. Rev. B* **40**, 546 (1989).
- [28] P. Buonsante, V. Penna, A. Vezzani, and P. B. Blakie, Mean-field phase diagram of cold lattice bosons in disordered potentials, *Phys. Rev. A* **76**, 011602(R) (2007).
- [29] L. Pollet, N. V. Prokof'ev, B. V. Svistunov, and M. Troyer, Absence of a direct superfluid to Mott insulator transition in disordered Bose systems, *Phys. Rev. Lett.* **103**, 140402 (2009).

- [30] S. Pal, R. Bai, S. Bandyopadhyay, K. Suthar, and D. Angom, Enhancement of the Bose glass phase in the presence of an artificial gauge field, *Phys. Rev. A* **99**, 053610 (2019).
- [31] A. Newell and J. C. Shaw, Programming the logic theory machine, in *Proceedings of the Western Joint Computer Conference* (Association for Computing Machinery, New York, 1957).
- [32] R. M. Ziff, P. T. Cummings, and G. Stells, Generation of percolation cluster perimeters by a random walk, *J. Phys. A: Math. Gen.* **17**, 3009 (1984).
- [33] R. M. Ziff, Hull-generating walks, *Physica D* **38**, 377 (1989).
- [34] J. Martín-Herrero, Hybrid object labelling in digital images, *Mach. Vis. Appl.* **18**, 1 (2007).
- [35] D. Jaksch, C. Bruder, J. I. Cirac, C. W. Gardiner, and P. Zoller, Cold bosonic atoms in optical lattices, *Phys. Rev. Lett.* **81**, 3108 (1998).
- [36] S. Braun, M. Friesdorf, S. S. Hodgman, M. Schreiber, J. P. Ronzheimer, A. Riera, M. del Rey, I. Bloch, J. Eisert, and U. Schneider, Emergence of coherence and the dynamics of quantum phase transitions, *Proc. Natl. Acad. Sci. USA* **112**, 3641 (2015).
- [37] M. Greiner, O. Mandel, T. Esslinger, T. W. Hänsch, and I. Bloch, Quantum phase transition from a superfluid to a Mott insulator in a gas of ultracold atoms, *Nature (London)* **415**, 39 (2002).
- [38] M. Greiner, O. Mandel, T. W. Hänsch, and I. Bloch, Collapse and revival of the matter wave field of a Bose-Einstein condensate, *Nature (London)* **419**, 51 (2002).
- [39] D. S. Rokhsar and B. G. Kotliar, Gutzwiller projection for bosons, *Phys. Rev. B* **44**, 10328 (1991).
- [40] K. Sheshadri, H. R. Krishnamurthy, R. Pandit, and T. V. Ramakrishnan, Superfluid and insulating phases in an interacting-Boson model: Mean-field theory and the RPA, *Europhys. Lett.* **22**, 257 (1993).
- [41] R. Bai, S. Bandyopadhyay, S. Pal, K. Suthar, and D. Angom, Bosonic quantum Hall states in single-layer two-dimensional optical lattices, *Phys. Rev. A* **98**, 023606 (2018).
- [42] S. Bandyopadhyay, R. Bai, S. Pal, K. Suthar, R. Nath, and D. Angom, Quantum phases of canted dipolar bosons in a two-dimensional square optical lattice, *Phys. Rev. A* **100**, 053623 (2019).
- [43] K. Suthar, H. Sable, R. Bai, S. Bandyopadhyay, S. Pal, and D. Angom, Supersolid phase of the extended Bose-Hubbard model with an artificial gauge field, *Phys. Rev. A* **102**, 013320 (2020).
- [44] R. Bai, D. Gaur, H. Sable, S. Bandyopadhyay, K. Suthar, and D. Angom, Segregated quantum phases of dipolar bosonic mixtures in two-dimensional optical lattices, *Phys. Rev. A* **102**, 043309 (2020).
- [45] K. Suthar, R. Kraus, H. Sable, D. Angom, G. Morigi, and J. Zakrzewski, Staggered superfluid phases of dipolar bosons in two-dimensional square lattices, *Phys. Rev. B* **102**, 214503 (2020).
- [46] H. Sable, D. Gaur, S. Bandyopadhyay, R. Nath, and D. Angom, Quantum quench dynamics of tilted dipolar bosons in 2D optical lattices, [arXiv:2106.01725](https://arxiv.org/abs/2106.01725).
- [47] B. Damski, The simplest quantum model supporting the Kibble-Zurek mechanism of topological defect production: Landau-Zener transitions from a new perspective, *Phys. Rev. Lett.* **95**, 035701 (2005).
- [48] B. Damski and W. H. Zurek, Adiabatic-impulse approximation for avoided level crossings: From phase-transition dynamics to Landau-Zener evolutions and back again, *Phys. Rev. A* **73**, 063405 (2006).
- [49] U. Bissbort, R. Thomale, and W. Hofstetter, Stochastic mean-field theory: Method and application to the disordered Bose-Hubbard model at finite temperature and speckle disorder, *Phys. Rev. A* **81**, 063643 (2010).
- [50] P. Pisarski, R. M. Jones, and R. J. Gooding, Application of a multisite mean-field theory to the disordered Bose-Hubbard model, *Phys. Rev. A* **83**, 053608 (2011).
- [51] Ş. G. Söyler, M. Kiselev, N. V. Prokof'ev, and B. V. Svistunov, Phase diagram of the commensurate two-dimensional disordered Bose-Hubbard model, *Phys. Rev. Lett.* **107**, 185301 (2011).
- [52] A. E. Niederle and H. Rieger, Superfluid clusters, percolation and phase transitions in the disordered, two-dimensional Bose-Hubbard model, *New J. Phys.* **15**, 075029 (2013).
- [53] Sk Noor Nabi and S. Basu, Percolation analysis of a disordered spinor Bose gas, *J. Phys. B: At. Mol. Opt. Phys.* **49**, 125301 (2016).
- [54] A. Barman, S. Dutta, A. Khan, and S. Basu, Understanding the Bose glass phase via a percolation scenario, *Eur. Phys. J. B* **86**, 308 (2013).
- [55] D. Clément, A. F. Varón, M. Hugbart, J. A. Retter, P. Bouyer, L. Sanchez-Palencia, D. M. Gangardt, G. V. Shlyapnikov, and A. Aspect, Suppression of transport of an interacting elongated Bose-Einstein condensate in a random potential, *Phys. Rev. Lett.* **95**, 170409 (2005).
- [56] D. Clément, P. Bouyer, A. Aspect, and L. Sanchez-Palencia, Density modulations in an elongated Bose-Einstein condensate released from a disordered potential, *Phys. Rev. A* **77**, 033631 (2008).
- [57] M. White, M. Pasienski, D. McKay, S. Q. Zhou, D. Ceperley, and B. DeMarco, Strongly interacting bosons in a disordered optical lattice, *Phys. Rev. Lett.* **102**, 055301 (2009).
- [58] B. S. Shastry and B. Sutherland, Twisted boundary conditions and effective mass in Heisenberg-Ising and Hubbard rings, *Phys. Rev. Lett.* **65**, 243 (1990).
- [59] R. Roth and K. Burnett, Superfluidity and interference pattern of ultracold bosons in optical lattices, *Phys. Rev. A* **67**, 031602(R) (2003).
- [60] N. Byers and C. N. Yang, Theoretical considerations concerning quantized magnetic flux in superconducting cylinders, *Phys. Rev. Lett.* **7**, 46 (1961).
- [61] M. Gerster, M. Rizzi, F. Tschirsich, P. Silvi, R. Fazio, and S. Montangero, Superfluid density and quasi-long-range order in the one-dimensional disordered Bose-Hubbard model, *New J. Phys.* **18**, 015015 (2016).
- [62] J. P. Álvarez Zúñiga, D. J. Luitz, G. Lemarié, and N. Laflorencie, Critical properties of the superfluid-Bose-glass transition in two dimensions, *Phys. Rev. Lett.* **114**, 155301 (2015).
- [63] R. F. Voss, The fractal dimension of percolation cluster hulls, *J. Phys. A: Math. Gen.* **17**, L373 (1984).
- [64] T. Grossman and A. Aharony, Structure and perimeters of percolation clusters, *J. Phys. A: Math. Gen.* **19**, L745 (1986).
- [65] T. Grossman and A. Aharony, Accessible external perimeters of percolation clusters, *J. Phys. A: Math. Gen.* **20**, L1193 (1987).
- [66] Anders Johansson, anjohan/fortperc: 0.1.0 (2022), <https://doi.org/10.5281/zenodo.6628467>.